

Editorial Manager(tm) JCOMP
Manuscript Draft

Manuscript Number:

Title: Data Assimilation with an Extended Kalman Filter
for Impact-Produced Shock-Wave Dynamics

Article Type: Regular Article

Keywords: Data Assimilation; Extended Kalman Filter; Shock-Wave
Dynamics; Hydrodynamic Code; Flyer Plate experiments; Error-Covariance Matrix;
Sequential Estimation; Quantification of Uncertainties; First-Order
Approximation

Corresponding Author: Jim Kao, PhD, Los Alamos National Laboratory

Other Authors: Dawn Flicker, Rudy Henninger, Sarah Frey, Michael Ghil,
Kayo Ide

LA-UR – 2003 –1278

**Data Assimilation with an Extended Kalman Filter
for Impact-Produced Shock-Wave Dynamics**

By

Jim Kao, Dawn Flicker and Rudy Henninger

Los Alamos National Laboratory

Sarah Frey

University of Arizona at Tucson

Michael Ghil¹ and Kayo Ide

University of California at Los Angeles

For submittal to Journal of Computational Physics

June 10, 2003

¹ Also affiliated with Ecole Normale Supérieure, Paris, France.

ABSTRACT

Model assimilation of data strives to determine optimally the state of an evolving physical system from a limited number of observations. The present study represents the first attempt of applying the extended Kalman filter (EKF) method of data assimilation to shock-wave dynamics induced by a high-speed impact. EKF solves the full nonlinear state evolution and estimates its associated error-covariance matrix in time. The state variables obtained by the blending of past model evolution with currently available data, along with their associated minimized errors (or uncertainties), are then used as initial conditions for further prediction until the next time at which data becomes available.

In this study, a one-dimensional (1-D) finite-difference code is used along with data measured from a 1-D flyer plate experiment. An ensemble simulation suggests that the nonlinearity of the modeled system can be reasonably tracked by EKF. The results demonstrate that the EKF assimilation of a limited amount of pressure data, measured at the middle of the target plate alone, helps track the evolution of all the state variables. The fidelity of EKF is further investigated with numerically generated synthetic data from so-called "identical-twin experiments", in which the true state is known and various measurement techniques and strategies can be made easily simulated. We find that the EKF method can effectively assimilate the density fields, which are distributed sparsely in time to mimic radiographic data, into the modeled system.

1. Introduction

Data assimilation has been used to estimate the state of a dynamic system by merging sparse data into a numerical model of the system [4, 7]. While any dynamic system in science and technology is potentially influenced by stochastic forcing, the complete state of the system can presumably be predicted in a computer code according to the system's underlying deterministic equations, subject to numerical errors and uncertainties associated with the initial condition and the time-independent model parameters. Meanwhile, observations, which represent the true state but are subject to sampling and measurement errors, may be available occasionally as a function of a subset of the system variables. Based upon a prognostic model, as described above, and a limited number of observations, Data assimilation attempts to provide a more comprehensive system analysis which may lead to a better prediction. This approach has proven particularly fruitful recently in the atmospheric and oceanic sciences [4, 8].

The extended Kalman filter (EKF) method [4, 7, 8, 14, 17, 22] was designed to perform data assimilation following the above prerequisites. There are two stages involved in the EKF: prediction and update. In the prediction stage, one solves the full nonlinear state evolution and, by using successive linearizations about the currently estimated state, advances the error covariance matrix in time. The update stage merges the model prediction and current observations, by giving each appropriate weights, to provide an “analyzed” or “assimilated” state. These weights are obtained through minimizing the trace of the error-covariance matrix (i.e., the mean-square errors) based on a probabilistic

analysis. The EKF thus provides a consistent first-order approximation to the optimal estimate of the nonlinear state at the observation time, as well as the errors of this estimate.

Data assimilation, in general, serves two purposes: better prediction and better understanding of the fundamental physics. If the underlying dynamics of a system is not fully known, DA may help develop a model of the system via parameter identification [23,24, 25]. Since this is the first study applying the EKF to shock-wave related research, we explore all the above aspects, starting from the feasibility test. We investigate the performance of EKF for simple flyer plate experiments in a one-dimensional (1-D) set-up where most of its nonlinearity is fairly well understood [1, 29]. The numerical model we use in this study is the 1-D version of the MESA code (MESA-1D) [27], which includes a sophisticated reconstruction of the material interface [28].

EKF is a nonlinear extension of the Kalman filter [17, 18] in 1960 that had originally been developed for linear systems with a small number of model unknowns [7,19]. Its application to continuum-mechanics problems [4] requires substantial computer storage and a large number of operations [21]. The EKF has been used, therefore, in the atmospheric and oceanic sciences often for idealized problems [14,22]. In applications to atmospheric, oceanic, and coupled models that are truly two- or three-dimensional (2-D or 3-D), some simplifications from the original EKF algorithm are necessary to reduce the computational burdens [9, 25]. The current study, therefore, serves also as a severe

test in applying EKF for a realistic problem represented by a 1-D configuration in shock dynamics.

The spatial and temporal distribution and the accuracy of observations are equally important factors in the performance of data assimilation. The observations may be linear or nonlinear, Eulerian or Lagrangian functions of the state variables. A convenient methodology, called as identical-twin experiments [4], generates synthetic data sets from controlled numerical experiments to test the usefulness of the data assimilation algorithms. As demonstrated in [15, 14], identical twin experiments are also a useful tool for observing system design, prior to actual measurements.

This paper is organized as follows. In Section 2 we give a brief review of the EKF method. Section 3 describes the MESA-1D code and the flyer plate experiments. Numerical results of applying EKF to actual experimental data appear in Section 4. Section 5 is devoted to “identical-twin experiments” where a density field that mimics radiographic imaging is synthetically generated and used for data assimilation. Concluding remarks appear in Section 6. A more complete description of the EKF algorithm is given in Appendix A. Appendix B describes some numerical aspects of implementing EKF in MESA-1D for flyer plate experiments.

2. The Extended Kalman Filter (EKF)

A detailed formulation of the EKF can be found in Gelb [7], Ghil and Malanotte-Rizzoli [8], Miller et al. [22] and Ide and Ghil [14]. A brief summary of the EKF method is given in this section, while the basic equations are listed in Appendix A for the interested readers. The notation follows Ide et al. [16], with some minor deviations motivated by the present application.

The EKF first predicts the state variables \mathbf{x}^p according to the system's deterministic equations, as a usual practice, where \mathbf{x} is an N -vector representing the state of the system (i.e., N is the number of the prognostic variables times the number of grid cells). The superscript 'p' stands for "predicted". The EKF then predicts the error-covariance matrix \mathbf{P}^p , defined by:

$$\mathbf{P}^p \equiv E [(\mathbf{x}^p - \mathbf{x}^t)(\mathbf{x}^p - \mathbf{x}^t)^T], \quad (2.1)$$

where E represents the expectation operator, \mathbf{x}^t represents the "true" state, and the superscript 'T' labels the transpose of a vector, using a matrix Riccati equation. The process described so far is straightforward and represents the EKF's prediction stage. The update stage is described below.

When observations become available, the EKF updates \mathbf{x}^p and \mathbf{P}^p to \mathbf{x}^a and \mathbf{P}^a , respectively, where the superscript ‘a’ stands for “assimilated”. Least-square minimization of $\text{tr}(\mathbf{P}^p)$, where tr is the trace of a matrix yields the Kalman gain matrix \mathbf{K} , which serves as a set of coefficient in weighting the so-called innovation vector, i.e. the difference between the actual observations and their model-predicted values.

The resultant \mathbf{x}^a and \mathbf{P}^a will be the initial conditions for the next cycle of prediction and update. The repetition of the prediction and update steps in time represents the sequential estimate of the system state and its uncertainties as obtained by the EKF. The performance of EKF can be measured by (1) evolution of $\text{tr}(\mathbf{P}^{p,a})$ that indicates the estimated least-square errors; (2) evolution of selected components of $\mathbf{P}^{p,a}$ that indicate how well the corresponding state variables are estimated in the least-square sense; and (3) comparison between the evolution of the observed and estimated state variables.

Both the system noise (or stochastic forcing) and solution errors due to numerical procedures and physical drawbacks have to be included in the prediction equation of \mathbf{P}^p as given information. The solution errors may be determined by validation runs of the model against existing data [13] or by ensemble runs of the model against an ultra-high-resolution reference run [6]. In the current application, we combine both kinds of errors into one single term as described in Appendix B.

3. MESA-1D Code and Flyer Plate Experiment

The Eulerian conservation equations for mass (ρ), momentum (u), internal energy (e), and the equation of state (EOS) in MESA-1D are expressed in the following using the total derivative D/Dt :

$$D\rho/Dt = -\rho u_x \quad (3.1)$$

$$\rho Du/Dt = -P_x \quad (3.2)$$

$$\rho De/Dt = -P u_x \quad (3.3)$$

$$P = p(\rho, e) + Q(\rho, \dot{\epsilon}) \quad (3.4)$$

where the subscript x represents the partial derivatives with respect to the spatial coordinate x , P is the total pressure which is the sum of the EOS pressure p and the artificial viscosity Q , and $\dot{\epsilon}$ is the total strain rate which is equal to u_x . In this work a solid phase Mie-Grüneisen EOS is used with the form of

$$p = p_H + \Gamma [\rho_0 e - 0.5 p_H (\mu/(1+\mu))] . \quad (3.5)$$

The Hugoniot pressure p_H is given by

$$p_H = [\rho_0 c_0^2 \mu(1+\mu)]/[1 - \mu(s-1)]^2 . \quad (3.6)$$

The artificial viscosity is defined as

$$Q = -C_L \rho c_0 \Delta x \dot{\epsilon} + C_Q \rho \Delta x^2 \dot{\epsilon}^2 . \quad (3.7)$$

The parameters in Eqs. (3.5) to (3.7) are defined as follows: Γ is the Grüneisen parameter, ρ_0 is the initial density, μ is the compression $\rho/\rho_0 - 1$, c_0 is the initial sound speed, Δx is the cell length, s is the shock velocity constant, and C_L and C_Q are artificial viscosity constants. MESA uses the third-order Van Leer's flux-limiting scheme [26] for advection

in order to maintain steep gradients without introducing large spurious oscillations. The material constitutive model for time-dependent deviatoric stresses is based on the classical elastic-perfectly-plastic treatment. The use of a ductile fracture (spall) model [1] is optional in the code.

The physical problem that we consider in this study is a 1-D flyer-plate experiment for which MESA-1D was used in a previous study [12]. A schematic diagram of the flyer-plate experiment is shown in Fig. 1a. The flyer plate with a velocity of $0.0645 \text{ cm } \mu\text{s}^{-1}$ (645 m s^{-1}) and a thickness of 0.3 cm impacts the stationary target plate that is 6 times thicker. This produces a shock that compresses the material to a Hugoniot pressure of about 20 Gpa at the impact plane. The shock waves travel into both plates with a speed of about $0.45 \text{ cm } \mu\text{s}^{-1}$, estimated from the Hugoniot data. These waves eventually reach the other boundaries of the plates, where they reflect back into the plate interiors as rarefaction waves. When they meet again at about $4.7 \text{ } \mu\text{s}$, tensile forces occur and may cause spallation (ductile fracture) inside of the target plate [1].

The computational domain includes two vacuum regions surrounding the copper plates to circumvent the potential problems due to boundary conditions of the plates. Our numerical simulations were performed using the model parameters summarized in Table 1. Figure 1b shows the x-t diagram of the experiment, which illustrates the loci of the shock-wave fronts, as obtained by the MESA-1D code for an $8 \text{ } \mu\text{s}$ simulation time without the spall treatment.

4. Pressure Data Assimilation

In this section, we assimilate the pressure data measured from a flyer plate experiment into MESA-1D using the EKF method. For the current study, we have pressure data collected at the middle of the target plate by a Manganin pressure gauge [3] between 2.0 to 3.8 μs (cf. Fig. 3). Therefore, most of the discussion regarding data assimilation with EKF is devoted to this time interval. The essential numerical considerations in implementing EKF into MESA-1D appear in Appendix B, including the linearization procedure and specifications of model and observation errors.

In order to verify whether the shock-wave dynamics of the 1-D flyer plate experiment is generally “tractable” by the MESA-1D code, we made an ensemble simulation with 100 realizations. This also helps shed light on the stability of the Jacobian calculations described in Appendix B. Each of the 100 realizations corresponds to a model run with a different stochastic forcing function represented by a different seeder of the random number generator described in Appendix B.

Figure 2 shows the time evolution of the model variables at the middle of the target plate for an 8 μs time frame from the ensemble simulation. We see, in general, a right-going shock wave followed by a left-going rarefaction wave, agreeing with the estimated shock speed of 0.45 $\text{cm } \mu\text{s}^{-1}$, mentioned in Section 3. The simulated pressure ensemble agrees

with the pressure data (cf. Fig. 3). It is apparent that internal energy tends to be most sensitive to the change in stochastic forcing; its dynamic range, however, is consistent with the kinetic energy inferred from the dynamic range of velocity evolution.

4.1. Evolution of Model Variables

Figure 3 shows the evolution of pressure with time at the middle of the target plate, as obtained by several distinct approaches. The corresponding curves are color-coded and identified in the figure caption. The pure prediction without any data assimilation (blue dash-dotted curve) exhibits numerical ringing (the Gibbs phenomenon) along its flat top portion, between 2.0 and 2.5 μs , due to the higher-order advection scheme. The difference between this curve and the actual data (green curve) is obvious, especially during the release-wave interval, where the pressure starts to decrease with time. The result of assimilating the pressure data with the EKF (solid black curve) agrees rather well with the data points in green. The result suggests that, with the given observation and model errors, the data carries more weight in the optimization process than the model. It even overcomes the numerical ringing during the flat top interval.

Note in Fig. 3 that there are three distinct time intervals with no data available: (i) 2.25 to 2.5 μs , (ii) 2.7 to 2.9 μs , and (iii) 3.1 to 3.45 μs . During each of these intervals, the model run with EKF is essentially making a prediction, based upon the updated information at the beginning of the interval, until the next update. For the first two intervals, the model

run with EKF does a credible prediction, as verified by comparing the prediction and the data points near the end of the time intervals.

As for the last interval that data are not available, the model run with EKF does not lead to a close matching of the next available data; instead, it coincides with the pure prediction as a result of the very similar initial conditions between the two cases during this interval. The sudden restoring feature at the end of this interval in the black curve shows that the EKF has very high confidence in the data. The further zig-zag variation in the black curve (from 3.5 to 4.0 μs) reflects the same situation. Namely, the prediction made by the EKF run between updates tends to stay away from the data until it is pulled back by the update process at each observation time.

It is clear from the above discussion that the pure prediction has a systematically sharper fall-off in pressure than the experimental data during the release-wave interval. As a result of applying data assimilation, the predicted pressure with EKF at the end of the simulation is about 12 kbar higher than the pure prediction. An additional simulation was made in which no more data points were used after the update at 3.4 μs (red dashed curve). This prediction for the rest of the simulation gradually merges to the blue dash-dotted curve that represents the pure prediction for the entire interval.

Figure 4 shows the effects of data assimilation with the pressure data on all the state variables: density, velocity, and internal energy at the middle of the target plate; pressure is repeated here for reference purposes. As stressed in Appendix B, pressure is not

considered as a state variable and is a given function of density and internal energy; i.e., equation of state (cf. Eq. (3.5) and (3.6)). As a result, these two state variables are affected by the assimilation of pressure data in a similar way as pressure itself is, especially over the flat-top interval. Due to the lack of an explicit dependence of pressure on velocity, the velocity field is affected less by the data assimilation, inasmuch as the difference between the pure prediction (blue dash-dotted curve) and the EKF run (solid black curve) is smaller.

Even though pressure was measured and assimilated only at the middle of the target plate, the effects of data assimilation are definitely not limited to this point, as shown in Fig. 5. This figure represents the averaged effects of EKF over the whole material domain except the interfaces. The results thus confirm the main virtues of the EKF for the highly nonlinear physics of shock-wave dynamics: (i) information trade-off between observed variables and unobserved; and (ii) propagation of information by the governing equations, from observed to unobserved locations [4, 8, 9].

4.2. Evolution of Uncertainties

As emphasized in Section 2, EKF performance can also be measured by the error covariance matrices. Figure 6 shows the global error with and without the EKF process. Due to the magnitude difference among the three state variables (cf. Figs. 7 and 8)), $tr(\mathbf{P}^p)$ is entirely dominated by the variances of density. Until data become available at

2.0 μs , the pure prediction results (blue dash-dotted curve) and those with data assimilation (black solid curve) coincide. The initial sudden drop in $\text{tr}(\mathbf{P}^p)$ shows merely that the initial value of \mathbf{P}^p was estimated too large by a factor of 3. After this initial adjustment of about 0.5 μs , the mean-square error increases slowly, with an approximately constant slope, due to the additive stochastic model error; see Eqs. (A.8) and (A.10).

When the pressure data become available, the mean-square error drops again suddenly, but only in the EKF run (black curve). During the interval of data availability, between 2.0 μs and 3.8 μs , the assimilation results have the same overall upward trend as the pure prediction results (blue curve), but run systematically lower and drop slightly each time when the pressure data becomes available. This shows that a single scalar observation can noticeably reduce the error in estimating the state of our system, with its total number of $3 \times \text{NC} = 222$ discrete variables.

At the end of the 4 μs simulation in Fig. 6, the RMS error, defined as $[\text{tr}(\mathbf{P}^p)/(\# \text{ of grid points})]^{0.5}$ is about 0.191×10^{-2} for the pure prediction case. For the case with EKF, the RMS error is 0.180×10^{-2} . For the case without the latest updates, the RMS error is 0.183×10^{-2} . There are, respectively, about 6 and 4 % improvements in the RMS error. Since density is the most dominant variable (cf. Fig. 7), these three RMS numbers may be considered as having units of gm cm^{-3} .

Figure 7 shows the variances for each individual state variable at the middle of the target plate as a function of time; these variances are simply the diagonal entities of \mathbf{P}^p at the appropriate grid point. Taking the square root of the values in Fig. 7 essentially provides error bars for Fig. 4. Each state variable in Fig. 7 carries a maximum variance near $2.0 \mu\text{s}$ for the pure prediction case, suggesting that the shock arrival (cf. Fig. 4) must significantly increase model errors in the system at hand. The data point of pressure near $1.9 \mu\text{s}$ effectively reduces the density variance from a maximum to nearly zero. A similar effect is seen in the internal energy variance. Due to the dependencies of pressure on density and internal energy, the variances of these two state variables at each up time are characterized by distinct but small-amplitude fluctuations.

Figure 8 shows the variances for each state variable at $3.02 \mu\text{s}$, at which time a pressure observation is available, as a function of grid location. The summation of all the values in Fig. 8 actually gives the $\text{tr}(\mathbf{P}^p)$ at $3.02 \mu\text{s}$, as included in Fig. 6. The two peaks in density variance, respectively located at grid points 32 and 52, correspond to the leading and trailing edges of the shock. Even though the pressure data is located at grid point 41, the effects of the EKF process reduce the errors at all other grid points and, most noticeably, at these two naturally sensitive spots.

4.3. Sensitivity to Model and Observation Errors

To compute the gain matrix \mathbf{K} as expressed by Eq. (A.7), the EKF accounts for both the model error (\mathbf{P}^p) and the observational error, denoted by \mathbf{R}^o , in the update procedure (see Section 2 and Appendix A). These two errors compete with each other as can be seen most easily from the scalar form of Eq. (A.7):

$$\mathbf{K} \sim \mathbf{P}^p / (\mathbf{P}^p + \mathbf{R}^o) = (1 + \mathbf{R}^o / \mathbf{P}^p)^{-1}. \quad (4.1)$$

It is seen that \mathbf{K} is basically the model error divided by the sum of itself and the observation error. If \mathbf{R}^o is relatively small with a fixed \mathbf{P}^p , \mathbf{K} will be relatively large; the same is the case if \mathbf{P}^p is large for a fixed \mathbf{R}^o . The assimilated variables are then more influenced by the observations than the predictions, cf. Eq. (A.4).

The EKF process does not always yield an optimized estimate that is as coincident with the data points as possible; it is not a data fitting process. The resultant optimal estimate is directly dependent on the model error \mathbf{Q}^p as well as the observation error \mathbf{R}^o , cf. Eq. (4.1). The case we demonstrated in Fig. 3 was based on the specific errors for the model and the data, as described in Appendix B.

If we increase the observation error from 0.1 kbar (as used in Fig. 3) to 1.0 kbar, the EKF results will be quite different assimilation, as depicted in Fig. 9a. The optimal estimate in this case considerably deviates from the data curve. The assimilation run

(black curve) lies much more closely to the pure prediction (blue) than the data curve (green), due to the smaller elements in the Kalman gain matrix \mathbf{K} . The final difference in pressure at $4.0 \mu\text{s}$ between cases with and without data assimilation is about 7 kbar in comparison with 12 kbar in Fig. 3. The overall uncertainties in the case of Fig. 9a are accordingly larger, due to a smaller \mathbf{K} , see Eq. (A.5).

We now consider the sensitivity of assimilated results to model error \mathbf{P}^p through the change of model's stochastic noise \mathbf{Q}^p according Eq. (A.2). Figures 9b and 9c show the assimilation results with the same observation error as in Fig. 9a but with a model error that is 2 and 10 times larger, respectively. By focusing on the later part of the simulation, a 2-times larger model error (Fig. 9b) helps bring the assimilated curve half-way closer to the data curve, while a 10-times larger model error recovers the original match shown in Fig. 3. As expected, these two cases would suffer, respectively, a 4-times and 100-times model uncertainty, compared with the case in Fig. 3. The above sensitivity study demonstrates that carefully assessing both the model and observation errors is crucial in obtaining meaningful results with the EKF method.

5. Observing System Assessment with Identical-Twin Experiments

Data assimilation can be tested without the need for real data: The identical-twin experiment is a numerical procedure where synthetic data can be generated by the model to which data assimilation is applied, subject to a specified stochastic forcing term [4, 8].

The data with assigned errors are then evaluated for their effectiveness in obtaining optimal state estimates. As demonstrated in [15, 9], such kind of numerical experiments can be a useful tool for designing an observing system prior to the actual measurements in meteorology and oceanography. Identical-twin experiments with this specific purpose were first carried out in planning the Global Atmospheric Research Program and were also called observing system simulation experiments (OSSE) [4].

To generate our synthetic data from a so-called control run, we integrate Eq. (A.8) to obtain \mathbf{x}^t with a given stochastic forcing \mathbf{q}^t . Its covariance matrix will be used as the \mathbf{Q}^p term in Eq. (A.2) for advancing \mathbf{P}^p . For more sophisticated measurements, the observation function \mathbf{h} in Eq. (A.4) may be complicated and extremely nonlinear. Radiographic imaging in 2-D of a 3-D experimental configuration is a good example in this regard [10, 11, 20]. For the current 1-D flyer plate experiments, the technology of measuring density through radiographic imaging is available but has not been fully investigated in the data assimilation context.

The radiographic data sets tend to cover the whole spatial extent of the materials but are relatively sparse in time. In this section, we demonstrate the effects of this technique using the EKF on synthetic data. For simplicity, we assume that radiography directly provides density data for the grid cells inside the target and flyer plates. We will thus be assimilating the entire density field into the code in the present experiment.

Figure 10 shows the EKF performance with the synthetic density data from grid points 12 to 63 available every $0.5 \mu\text{s}$ (i.e., every 50 time steps; see Table 1). These 52 grid cells are chosen for their being well within the material, as explained in Appendix B about the interface between material and vacuum. The stochastic forcing used to generate \mathbf{x}^t in time is based on the same random distribution functions as described in Appendix B. The synthetic density data sets are constructed based on Eq. (A.10) with a random error distribution within $\pm 0.5 \text{ gm cm}^{-3}$ (about 5 % of the ambient value of density). The graphs in Fig. 10 show the spatially averaged model variables over the 52 grid points where data were assumed to be present, for a simulation time of $8.0 \mu\text{s}$; this time interval basically covers a compression period as well as a tensile period (see Section 3).

Figure 10 shows that assimilation of density field leads to both this field and the pressure field (black curves) following very closely the synthetic data (red dashed curves). The stochastic forcing generates some mass inside the 52 material grid cells during the compression period and leads to some mass loss during the tensile period, when comparing the pure prediction (blue dash-dotted curve) and the stochastically forced run (red dashed curve) in the density panel of Fig.10. There are, in fact, no net changes of mass and pressure between these two runs, which shows that the stochastic forcing has been carefully implemented. Both velocity and internal energy, however, show decreased magnitudes in a time-integrated sense for the stochastically forced run. The effect of the EKF assimilation on the velocity field seems to over-correct it somewhat, while the effect on internal energy is more uniformly positive.

Figure 11 plots the global error in terms of $tr(\mathbf{P}^p)$ for the case of synthetic-density assimilation. Because nearly the whole density field is assimilated, and density is the dominant variable in terms of dimensional size (recall Section 4.2), the global error is close to zero at the update times. During the time intervals without data, the growth of the error is characterized by two stages. The first stage is steep and dominated by the imposed stochastic forcing \mathbf{Q}^p , while the second stage is much less steep and due to the combined effect of \mathbf{Q}^p and the system's deterministic error growth, represented by the blue dash-dotted curve.

The red dashed curves represent the growth of the error if the data at 1.5 (or 2.5 or 3.5) μs and later were not available. These curves illustrate the continued error evolution of the second stage, as just explained. The blue dashed curve represents the case of only one data set being available, at 3.5 μs . Since taking radiographic data is an expensive process, the present OSSEs are useful in determining the best timing of taking such data, so they can be most cost-effective in terms of the final errors (or uncertainties). The results shown in Fig. 11 suggest that, if limited to a small number of radiographic data takings, it is more beneficial to take the data at a later time.

6. Concluding Remarks

This paper described applications of data assimilation to a simple, but realistic 1-D hydrodynamic model of shock behavior induced by a high-speed impact. Sequential

estimation was introduced for small-dimensional systems, such as rocket navigation, in the early 1960s [7, 17, 18, 19]. It has become wide-spread in fluid-dynamical problems posed by very large atmospheric and oceanic models with a severely limited amount of data over the last two decades [4, 8, 9, 16, 21]. The extended Kalman filter (EKF) method [8, 17, 14, 22] was employed in the current study for assimilating data into the MESA-1D code [27]. EKF was designed to optimize predictions of, as well as reduce uncertainties in, the modeled state variables, provided that the errors of observations and model performance are known.

The EKF algorithm solves the full nonlinear state evolution and its associated error-covariance matrix in time. It provides a consistent first-order approximation to the optimal estimate of the state and of the time-dependent model uncertainties, both when data are available and when they are not.

A limited amount of experimental data was available for this study from a 1-D flyer plate experiment (Fig. 1). Before the actual implementation of EKF, we conducted an ensemble simulation of 100 realizations to explore the potential effect of model uncertainties. These simulations (Fig. 2) showed that the potential effects of random uncertainties are largest in the system's internal energy. The EKF results, in general, demonstrate that pressure data at the middle of the target plate alone helps track the evolution of all the state variables (Figs. 3 to 8). After the model update at observation time, the "assimilated" state variables and their associated minimized errors are used as initial conditions for a fresh start of model prediction till the next data time, or, if data is

no longer available, till any desired future time. For shock-wave related research or applications, the EKF thus provides important additional information where experimental data are missing, in part or altogether.

When available, data sets should not be used only for validating current model performance, but also to predict certain scenarios for which it is not possible at present to obtain any data. This is especially true for risk assessments or vulnerability analyses. Good examples include future climate change and nuclear weapon stockpile stewardship.

EKF was further used for the purpose of observing-system design in our 1-D shock-wave context. To do so, we generated synthetic data numerically from identical-twin experiments. In such experiments, the “true” state is obtained from a “control run” of the stochastically disturbed deterministic model, which can then provide the simulation of a desired measurement pattern. We found that a small number of density field updates, such as might be provided by radiographic data sets, can effectively track the solution through a large reduction of model errors.

To the best of our knowledge, there has been no previous attempt to use data assimilation in high-speed impact studies or solid mechanics modeling. We have shown here how this approach can expand and refine our knowledge in these fields using the limited laboratory data available. Using the same methodology, we expect to use the EKF for the optimal estimation of physical parameters in fracture problems. We will utilize the

Manganin pressure data [3], as well as velocity data based on the VISAR interferometer [2] and radiographic data [20].

ACKNOWLEDGMENTS

The authors are thankful for technical discussions with Dimitri Kondrashov, Ken Hanson, Len Margolin, Bill Powers, and Arch Thiessen. The Institute of Geophysics and Planetary Physics (IGPP) at Los Alamos National Laboratory (LANL) provides administrative assistance in the collaboration between LANL and UCLA. This project is under the auspices of the US Department of Energy.

APPENDIX A

General Extended Kalman Filter (EKF) Algorithm

For a complete derivation of the EKF algorithm, Readers are referred to [7, 8, 17]. In this appendix we merely list the equations, as used in the present study. Specific numerical issues of implementation in the MESA-1D code are addressed in Appendix B. The prediction stage of the EKF method is as follows:

$$D\mathbf{x}^p = \mathbf{m}(\mathbf{x}^p) Dt \quad , \quad (\text{A.1})$$

$$d\mathbf{P}^p = [\mathbf{M}^p \mathbf{P}^p + \mathbf{P}^p (\mathbf{M}^p)^T + \mathbf{Q}^p] dt , \quad (\text{A.2})$$

where D/Dt is the total derivative, $\mathbf{m}(\mathbf{x}^p)$ represents the governing deterministic processes, and the Jacobian matrix \mathbf{M}^p in the linear system of ordinary differential equations (ODEs) of Eq. (A.2) is defined as:

$$\mathbf{M}^p \equiv (\partial m_k / \partial x_l)_{\mathbf{x}=\mathbf{x}^p} . \quad (\text{A.3})$$

Equation (A.3) represents the linearized transition matrix and m_k and x_l are the k th and l th components of the deterministic processes \mathbf{m} and state variables \mathbf{x} , respectively. The matrix \mathbf{Q}^p in Eq. (A.2) is the estimated system noise covariance for the prediction of \mathbf{P}^p ; see Eq. (A.9) below.

When observations are available, the EKF updates \mathbf{x}^p to \mathbf{x}^a and \mathbf{P}^p to \mathbf{P}^a by:

$$\mathbf{x}^a = \mathbf{x}^p + \mathbf{K} [\mathbf{y}^o - \mathbf{h}(\mathbf{x}^p)], \quad (\text{A.4})$$

$$\mathbf{P}^a = (\mathbf{I} - \mathbf{K}\mathbf{H}) \mathbf{P}^p, \quad (\text{A.5})$$

where \mathbf{y}^o and \mathbf{h} , respectively, represent the observations and the observation functions, explained by Eqs. (A.11) to (A.13) below, \mathbf{K} is the Kalman gain matrix described by Eq.

(A.7), \mathbf{P}^a is the error-covariance matrix defined by $\mathbf{P}^a \equiv E [(\mathbf{x}^a - \mathbf{x}^t)(\mathbf{x}^a - \mathbf{x}^t)^T]$, \mathbf{I} is the identity matrix, and \mathbf{H} is the Jacobian of \mathbf{h} , which is defined by:

$$\mathbf{H} \equiv (\partial h_k / \partial x_l)_{\mathbf{x}=\mathbf{x}^p} . \quad (\text{A.6})$$

Equation (A.6) represents the linearized observation matrix, where h_k and x_l are the k th and l th components of \mathbf{h} and \mathbf{x} , respectively. The Kalman gain matrix \mathbf{K} in Eqs. (A.4) and (A.5) is obtained by minimizing $tr(\mathbf{P}^a)$; the result of this minimization [7, 8] is

$$\mathbf{K} = \mathbf{P}^p \mathbf{H}^T (\mathbf{H} \mathbf{P}^p \mathbf{H}^T + \mathbf{R}^o)^{-1} \quad (\text{A.7})$$

where \mathbf{R}^o is the covariance matrix of the observation error; see Eqs. (A.11) to (A.13) below.

The prediction stage described by Eqs. (A.1) to (A.3) and the update stage given by Eqs. (A.4) to (A.7) together constitute the EKF algorithm for estimating the ‘true’ state of the system, governed by a nonlinear stochastic differential equation,

$$D\mathbf{x}^t = \mathbf{m}(\mathbf{x}^t) Dt + d\mathbf{q}^t ; \quad (\text{A.8})$$

in Eq. (A.8), the stochastic forcing $d\mathbf{q}^t$ is assumed to represent unknown model errors (such as subgrid-scale processes) and is given by an N-dimensional Wiener process,

$$\mathbf{q}^t \sim N(0_N, \mathbf{Q}^t), \quad (\text{A.9})$$

with zero mean and a covariance matrix \mathbf{Q} defined as:

$$\mathbf{Q} \equiv E[\mathbf{q} \mathbf{q}^T]; \quad (\text{A.10})$$

see the last paragraph in Appendix B for the actual prescription of $d\mathbf{q}^t$ used in the model.

While the “true” state \mathbf{x}^t evolves according to Eqs. (A.8) and (A.9), several observations \mathbf{y}^o regarding this system become available and \mathbf{y}^o is represented by:

$$\mathbf{y}^o = \mathbf{y}^t + \mathbf{w}^o, \quad (\text{A.11})$$

here \mathbf{y}^o is an M -vector of observations contaminated by white noise \mathbf{w}^o that represents observational errors, which occur in measuring \mathbf{y}^t , and are assumed to have zero mean and unknown covariance matrix \mathbf{R}^o :

$$\mathbf{w}^o \sim N(0_M, \mathbf{R}^o), \quad (\text{A.12})$$

with $\mathbf{R} \equiv E[\mathbf{w} \mathbf{w}^T]$. The (unknown) “true” observations \mathbf{y}^t are connected to the true state \mathbf{x}^t by

$$\mathbf{y}^t = \mathbf{h}(\mathbf{x}^t), \quad (\text{A.13})$$

where \mathbf{h} is an M -vector of observation functions that, linearly or nonlinearly, depend on the state variables \mathbf{x} .

In summary, for an N -vector of state variables \mathbf{x} and an M -vector of observations \mathbf{y}^o , where typically $M \ll N$, \mathbf{P}^p and \mathbf{P}^a are $N \times N$ error-covariance matrices of the state variables, \mathbf{Q}^p is an $N \times N$ covariance matrix of model errors (or unresolved stochastic forcing), \mathbf{M}^p is an $N \times N$ linearized transition matrix, \mathbf{H} is an $M \times N$ linearized observation matrix, \mathbf{K} is an $N \times M$ Kalman gain matrix, and \mathbf{R}^o is an $M \times M$ covariance matrix of observational errors.

APPENDIX B

Numerical Aspects of Implementing EKF in MESA 1-D

This section describes a perturbation method for the calculation of the Jacobian matrix given in Eq. (A.3), which represents the linearization process within EKF. Prior to our work, the MESA-1D code has been used for sensitivity analysis with respect to the model parameters listed in Table 1. To apply the differential sensitivity approach to such an analysis, the automatic differentiation computer program called ADFOR [5] was successfully tested in MESA-1D [12]. In principle, ADFOR can be used for the calculation of the Jacobian matrices \mathbf{M}^p ; see Eq. (A.3) in the Appendix A. However,

since the N-vector of deterministic functions \mathbf{m} in Eq. (A.1) is not given analytically in closed mathematical form, difficulties arise in using an automatic differentiation program for the Jacobian calculations.

Instead, we use a straightforward perturbation method in which $m(x)^n$ is first defined as

$$m(x)^n \equiv (x^{n+1} - x^n) / \Delta t, \quad (\text{B.1})$$

where superscript ‘n’ represents the time step and Δt is the size of the time step (see Table 1). We then perturb each element of \mathbf{x}^n with the machine precision parameter $\varepsilon = 10^{-7}$ to obtain $m(x+\varepsilon)^n$. Finally, Eq. (A.3) can be simply represented by

$$\mathbf{M}^p \equiv \{ [m(x+\varepsilon) - m(x)]_k / \varepsilon \}_{x=\mathbf{x}^p}. \quad (\text{B.2})$$

This method essentially requires (N+1) simulations, where N is the total number of unknowns. While only an approximation, it is actually not more computationally intensive than the automatic differentiation and requires far less debugging.

It turns out that this perturbation approach works very effectively except at the interfaces between the copper plates and the vacuums (i.e., at the material boundaries), where large values of Jacobian, calculated from Eq. (B.2), may cause instabilities in the integration of Eq. (A.2). While such instabilities are undesirable, the interface is indeed a physically and numerically unstable region in most of Eulerian numerical codes. To avoid this

problem, we simply skip the interfaces as well as the attached vacuum regions (to avoid round-off errors in the latter case) in the integration of Eq. (A.2). Namely, no EKF is performed for the grid cells at the two ends of the computational domain, which represent the vacuums and the interfaces.

When the observation functions \mathbf{h} in Eq. (A.4) are nonlinear functions of \mathbf{x} , that are given only numerically, and not analytically, the observation Jacobians \mathbf{H} (see Eq. (A.6)) can be determined the same way as described above for \mathbf{M}^p . The pressure data used for the current assimilation is a function of density and internal energy through the equation of state; Eqs. (3.5) and (3.6). Therefore, analytical expressions are available for \mathbf{H} and there is no need for a numerical approximation.

In atmospheric and oceanic applications, an initial \mathbf{P}^p is estimated in order to integrate Eq. (A.2). For modeling a laboratory experiment, as in the current study, the initial \mathbf{P}^p can be set to be zero. The matrix \mathbf{Q}^p in Eq. (A.2) is constructed based on Eq. (A.10). We assume that \mathbf{q} in Eq. (A.10) represents the combination of the system and solution errors and is expressed as a random distribution function on grid cells, with magnitudes between $\pm 10^{-3} \times \Phi$, where Φ represents the reference values of each state variable. In other words, the linear changes of each state variable due to $d\mathbf{q}$ alone in Eq. (A.8) would be within $\pm 100\%$ of Φ after 1000 time-steps of integration. In the current case, Φ is set to be 10.0 gm cm^{-3} , $10^{-1} \text{ cm } \mu\text{s}^{-1}$, and $10^{-3} \text{ Mbar.cc.gm}^{-1}$, respectively, for density, velocity, and internal energy. Finally, the observation error of the pressure data measured by the

Manganin pressure gauge is assumed to be 10^{-1} kbar (cf. Section 4.3 for its sensitivity tests).

References

[1] Addessio, F. L., and J. N. Johnson, 1993: Rate-dependent ductile failure model. *J. Appl. Phys.*, 74, 1640-1648.

[2] Baker L. M., and R. E. Hollenbach, 1972, *J. Appl. Phys.*, 11, 4669.

[3] Baker K. M., M. Shahinpoor, and L. C. Chhabildas, 1993, in *High-Pressure Shock Compression of solids*, J. R. Asay and M. Shahinpoor Eds., Springer-Verlag Press, p43.

[4] Bengtsson, L., M. Ghil, and E. Källén (Eds.), 1981: *Dynamic Meteorology: Data Assimilation Methods*, Springer-Verlag, New York/Heidelberg/Berlin, 330 pp.

[5] Bischof, C., A. Carle, P. Khademi, and A. Mauer, 1995: *The ADFOR 2.0 system for the automatic differentiation of Fortran 77 programs*. Argonne National Laboratory Report, ANL-MCS-P481-1194.

- [6] DeVolder, B., J. Glimm, J. W. Grove, Y. Kang, K. Pao, D. H. Sharp, 2002: A statistical study of errors in simulations of shock wave interaction. Los Alamos Unclassified Release. LA-UR-01-3671.
- [7] Gelb, A. (Ed.), 1974: Applied Optimal Estimation. The MIT Press, 347pp.
- [8] Ghil, M., and Malanotte-Rizzoli, P., 1991: Data assimilation in meteorology and oceanography. *Adv. Geophys.*, 33, 141-226.
- [9] Ghil, M., 1997: Advances in sequential estimation for atmospheric and oceanic flows. *J. Meteor. Soc. Japan*, 75, 289–304.
- [10] Grunbaum, F. A., 1982: Limited angle reconstruction problems in X-Ray and NMR tomography *P. Soc. Photo-Opt. Inst.*, 372, 185-187.
- [11] Grunbaum, F. A., 2001: A nonlinear inverse problem inspired by three-dimensional diffuse tomography. *Inverse Probl.*, 17, 1907–1922.
- [12] Henninger, R. J., P. J. Maudlin, and M. L. Rightley, 1997: Accuracy of differential sensitivity for one-dimensional shock problems. APS Shock Compression of Condensed Matter Conference, Amherst, MA.

- [13] Hills, G. R., and T. G. Trucano, 2001: Statistical validation of engineering and scientific models with application to CTH. Sandia National Laboratory Rep., SAND2001-0312, 118pp.
- [14] Ide, K., and M. Ghil, 1997a: Extended Kalman filtering for vortex systems. Part I: Methodology and point vortices. *Dyn. Atmos. Oceans*, 27, 301-332.
- [15] Ide, K., and M. Ghil, 1997b: Extended Kalman filtering for vortex systems. Part II: Rankine vortices and observing-system design. *Dyn. Atmos. Oceans*, 27, 333–350.
- [16] Ide, K., P. Courtier, M. Ghil, and A. Lorenc, 1997: Unified notation for data assimilation: Operational, sequential and variational. *J. Meteor. Soc. Japan*, 75, 181–189.
- [17] Jazwinski, A. H., 1970: *Stochastic Processes and Filtering Theory*, Academic Press, New York, 376 pp.
- [18] Kalman, R. E., 1960: A new approach to linear filtering and prediction problems. *Trans. ASME, Ser. D, J. Basic Eng.*, 82D, 35-45.
- [19] Kalman, R. E., and R. S. Bucy, 1961: New results in linear filtering and prediction problems. *Trans. ASME, Ser. D, J. Basic Eng.*, 83D, 95-108.

- [20] Kwan, T., A. Mathews, P. Christenson, and C. Snell, 2001: Integrated system simulation in X-ray radiography. *Computer Phys. Communications*, 142, 263-269.
- [21] Lyster, P. M., S. E. Cohn, R. Menard, L.-P. Chang, S. -J. Lin, and R. Olsen, 1997: Parallel implementation of a Kalman Filter for constituent data assimilation. *Mon. Wea. Rev.*, 125, 1674-1686.
- [22] Miller, R., Ghil, M., Gauthiez, F., 1994: Advanced data assimilation in strongly nonlinear dynamical systems. *J. Atmos. Sci.*, 51, 1037-1056.
- [23] Navon, I. M., 1998: Practical and theoretical aspects of adjoint parameter estimation and identifiability in meteorology and oceanography, *Dynam. Atmos. Oceans*, 27, 55-79.
- [24] Smedstad, O. M., and J. O'brien, 1991: Variational data assimilation and parameter estimation in an equatorial Pacific ocean model. *Prog. Oceanogr.*, 26, 179-241.
- [25] Sun, C., Z. Hao, M. Ghil, and J. D. Neelin, 2002: Data assimilation for a coupled ocean-atmosphere model. Part I: Sequential state estimation. *Mon. Wea. Rev.*, 130, 1073-1099.
- [26] Van Leer, B., 1979: Towards the ultimate conservation difference scheme. V. A second-order sequel to Godunov's method. *J. Comp. Phys.*, 32, 101-135.

[27] Cagliostro, D. J., D. A. Mandell, L. A. Schwalbe, T. F. Adams, and E. J. Chapyak, 1990: MESA 3-D calculations of armor penetration by projectiles with combined obliquity and yaw, *Int. J. Impact Engineering*, 10.

[28] Youngs, D. L., 1987: An interfacing tracking method for a 3-D Eulerian hydrodynamics code. UK Atomic Weapons Establishment, AWRE/44/92/35.

[29] Zukas, J. A. (Ed.), 1990: *High Velocity Impact Dynamics*. John Wiley & Son Press, 935pp.

Figure Legends

Fig. 1. (a) A schematic diagram of the 1-D flyer plate experiment (see Table 1 for parameter specifications); and (b) the space-time diagram of the simulated shock represented by pressure from the MESA-1D code (cf. Fig. 2).

Fig. 2. Model variable evolution in 100 runs with different stochastic forcing function realizations. Each forcing function realization corresponds to a different seeding of the random distribution described in Appendix B. The four panels correspond to density,

velocity, internal energy, and pressure; the same ordering of the panels is maintained in all similar figures below.

Fig. 3. Pressure evolution at the middle of the target plate with an observation error (w) of 0.1 kbar and a normalized model error (q) of 0.001 (see Appendix B). Green curve: fitted to the experimental data points marked by green circles; blue dash-dotted curve: pure prediction without EKF; black solid curve: assimilated evolution with EKF; red dashed curve: the evolution that the black curve would have undergone if no data were available after 3.4 μs .

Fig. 4. Time evolution of all the state variables (density, velocity, and internal energy) and the pressure for the same simulation and at the same location as depicted in Fig. 3. Refer to Fig. 3 for curve legends.

Fig. 5. The same as Fig. 4 except for spatially averaged time evolution over all material grid points. Blue dash-dotted curve: pure prediction without EKF; and black solid curve: assimilation with EKF.

Fig. 6. The trace of \mathbf{P}^p (the sum of the variances) as a function of time. Blue dash-dotted curve: pure prediction without EKF; black solid curve: assimilated evolution with EKF; red dashed curve: the evolution that the black curve would have undergone if no data were available after 3.4 μs . The blue and black curves coincide with each other until the first data point at 1.9 μs .

Fig. 7. The variances of the three state variables at the middle of the target plate as a function of time. Refer to Fig. 6 for the legends of different curves.

Fig. 8. The variances of the three state variables at the data (or update) time of $3.02 \mu\text{s}$ as a function of grid location. Blue dash-dotted curve: pure prediction without EKF; and black solid curve: assimilation result with EKF just after the update.

Fig. 9. The same as Fig. 3 except with (a) 10 times larger of observation errors; (b) 10 times larger of observation errors and 2 times larger of model errors; and (c) 10 times larger of observation errors and 10 times larger of model errors.

Fig. 10. Time evolution for all the state variables and the pressure, spatially averaged over material grid points when assimilating synthetic density fields. Blue dash-dotted curve: pure prediction without EKF; black solid curve: assimilation with EKF; and red dashed curve: synthetic data from the “control run”.

Fig. 11. The trace of \mathbf{P}^D as a function of time in the identical-twin experiment. Blue dash-dotted curve: pure prediction without EKF; and black solid curve: assimilated evolution with EKF. The red dashed curves represent the evolution that the black curve would have undergone if no density data were available after 1.49 or 2.49 or $3.49 \mu\text{s}$, respectively; the blue dashed curve represents the case in which there is only one data set available, at $3.5 \mu\text{s}$.

Table 1: Model Parameters

Parameter	Description	Value
NC	Total number of grid cells	74
Δx	Grid size	0.0375 cm
$(NC)_{\text{flyer}}$	Number of grid cells in flyer plate	8
$(NC)_{\text{target}}$	Number of grid cells in target plate	48
$(NC)_{\text{vacuum}}$	Number of grid cells in vacuum regions	18 (9 x 2)
Δt	Maximum size of time step	0.01 μs
$\rho(t=0)$	Initial density	8.93 gm cm^{-3}
$u_{\text{fp}}(t=0)$	Initial velocity of flyer plate	0.0645 $\text{cm } \mu\text{s}^{-1}$
Y	Yield stress	0.026 Mbar
G	Shear modulus	0.46 Mbar
Γ	Gruneisen parameter	2.002
s	Shock velocity constant	1.489
c_0	Initial sound speed	0.394 $\text{cm } \mu\text{s}^{-1}$
C_L	Linear artificial viscosity constant	0.2
C_Q	Quadratic artificial viscosity constant	2.0

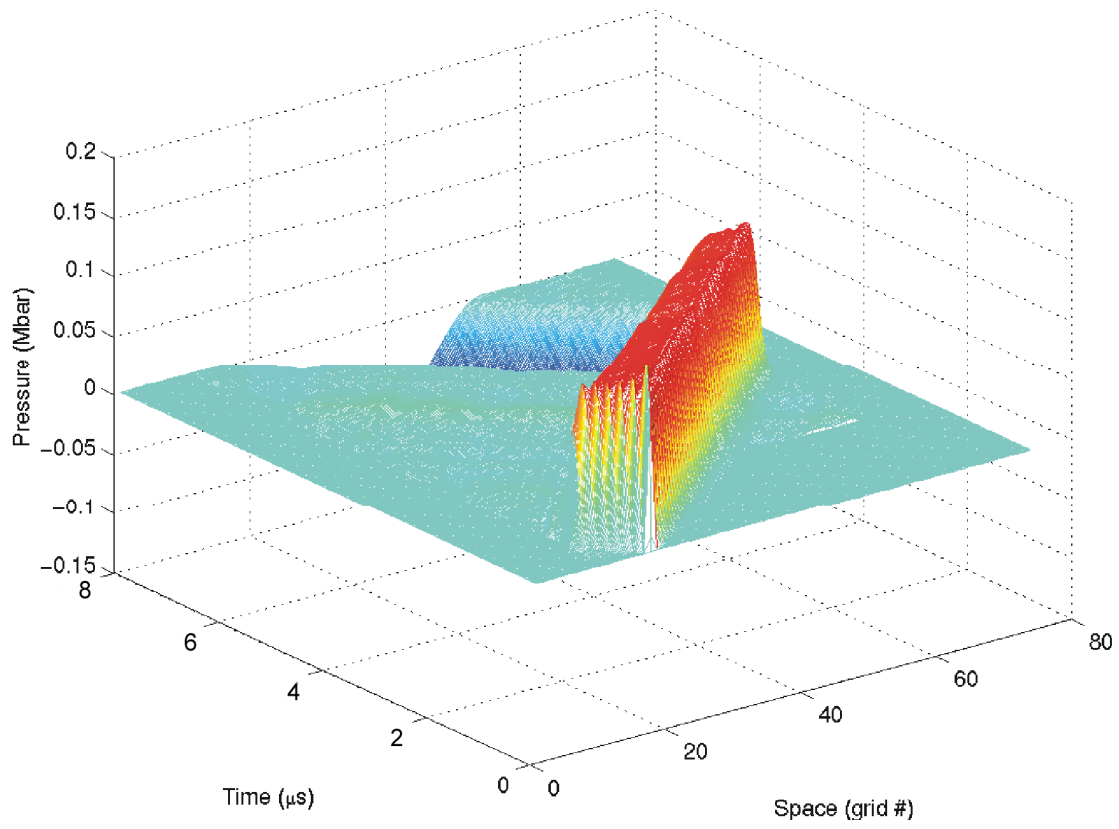
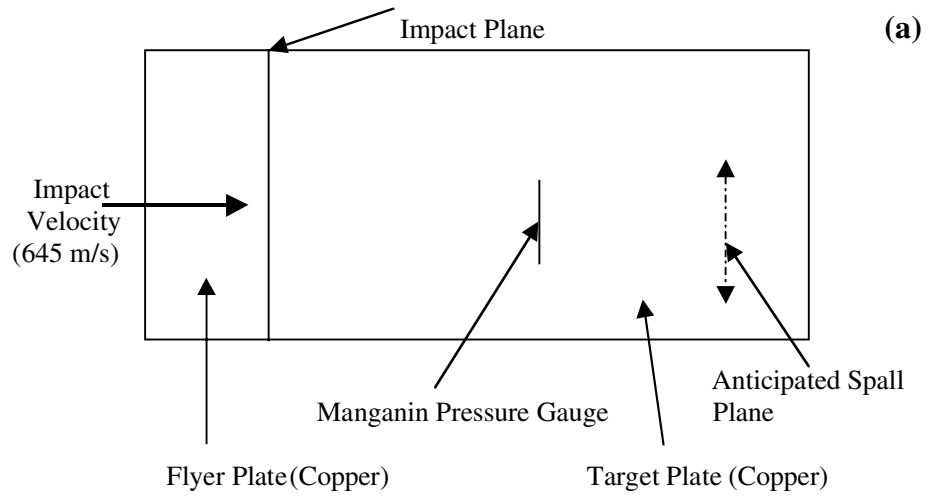


Fig. 1

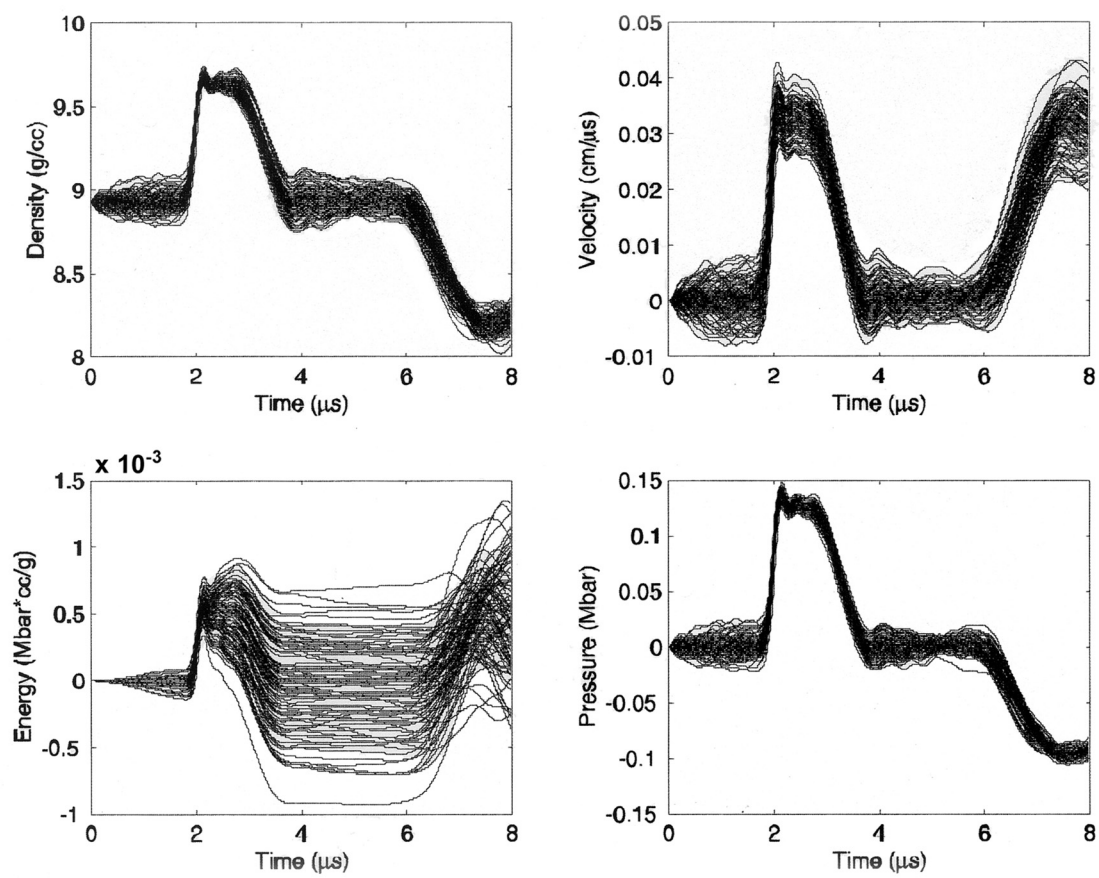


Fig. 2

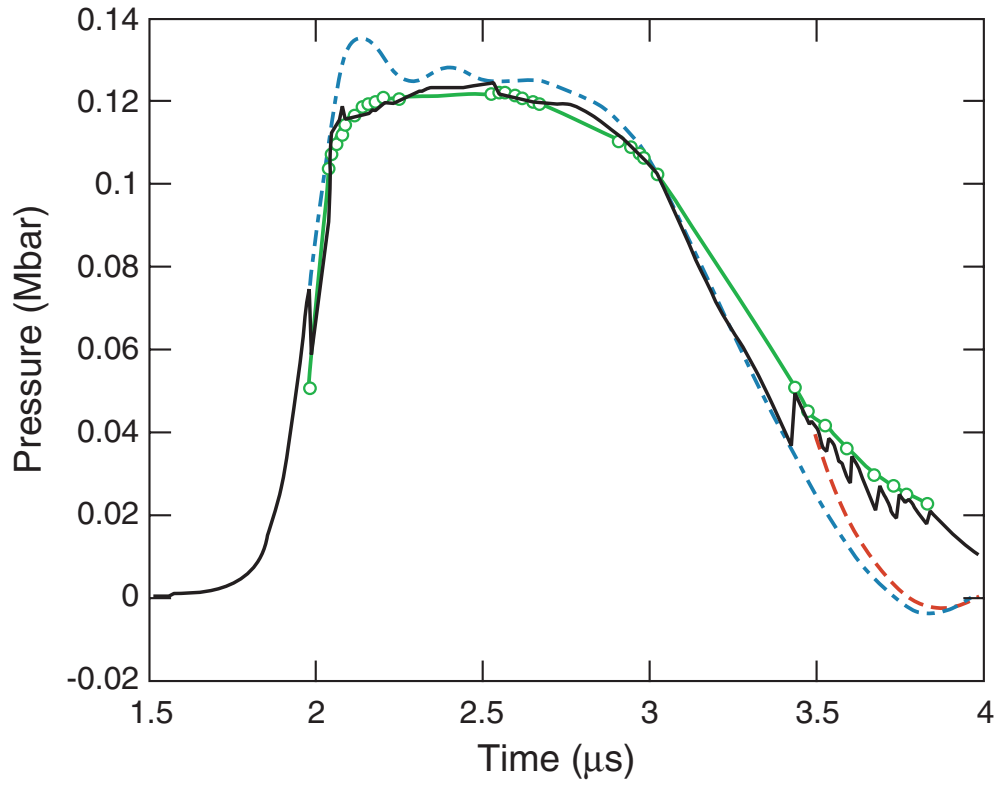


Fig. 3

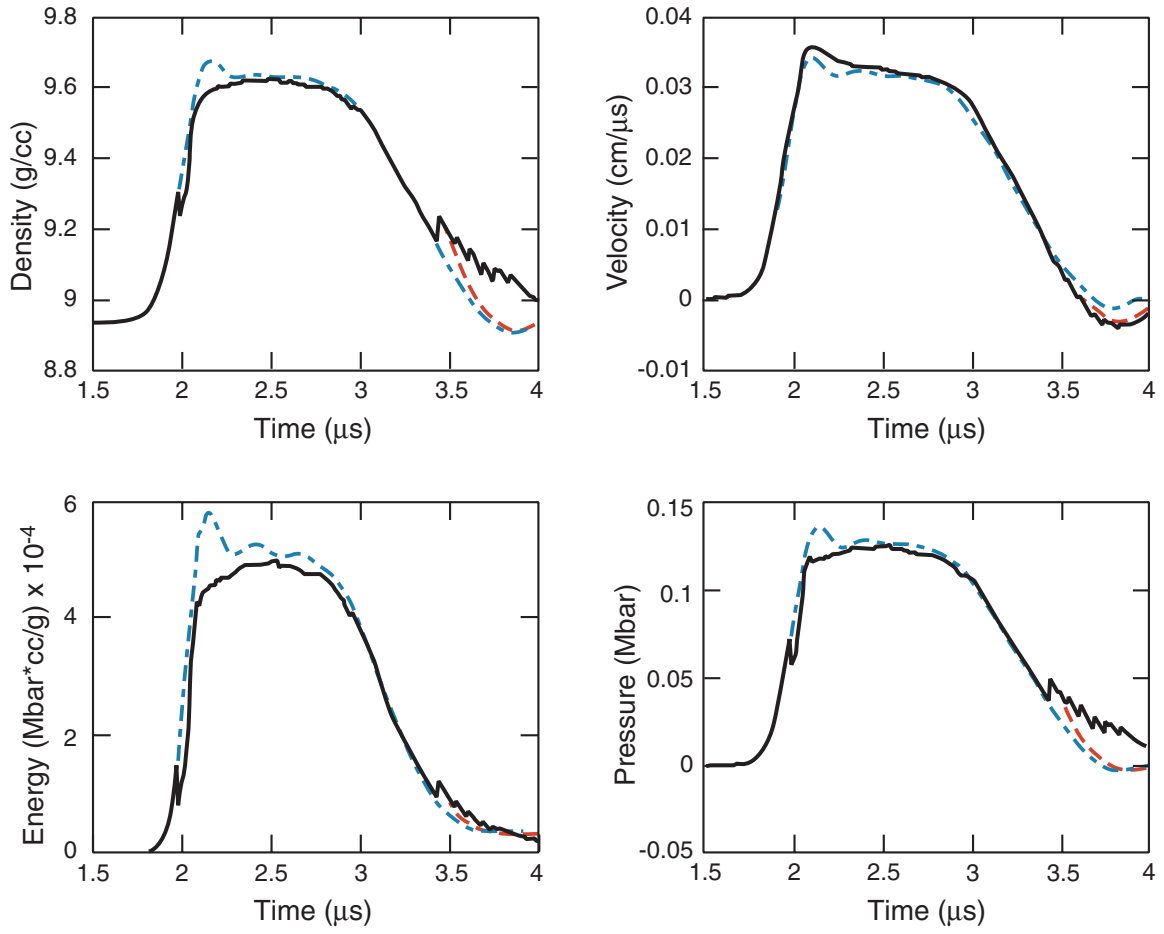


Fig. 4

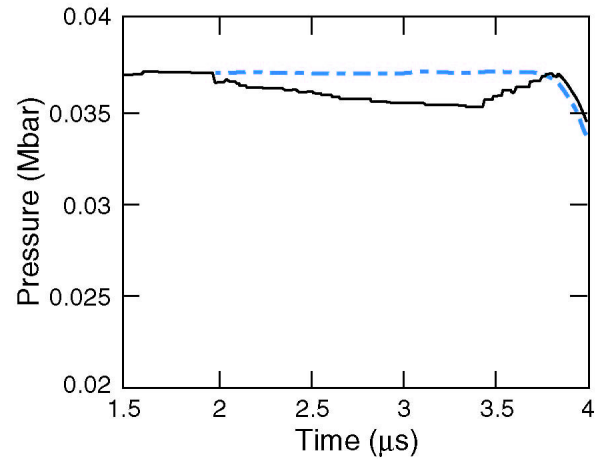
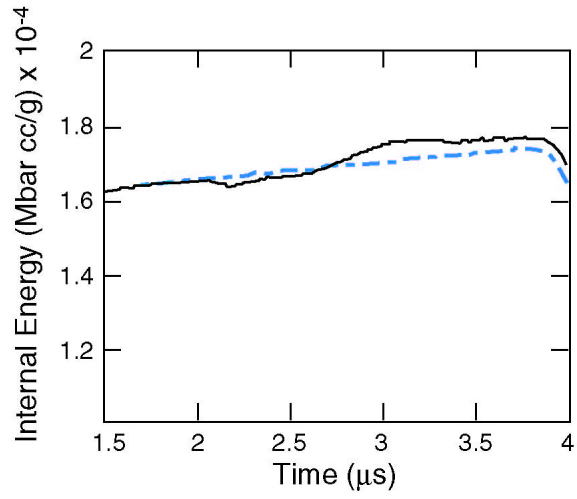
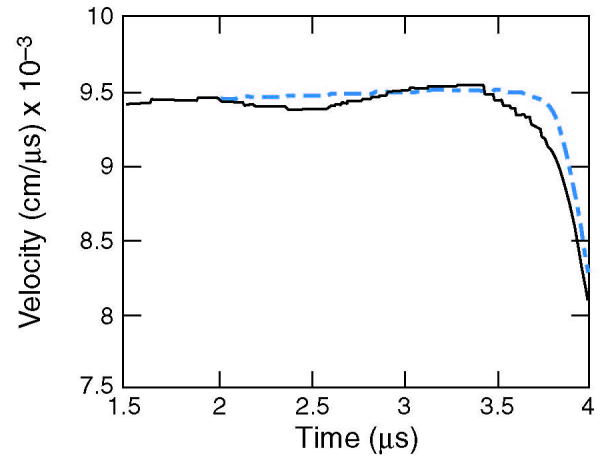
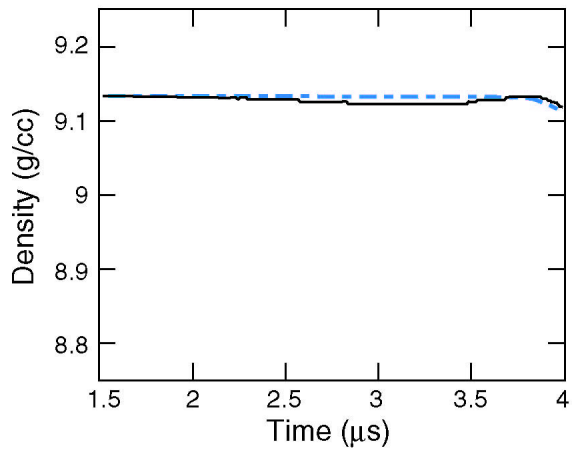


Fig. 5

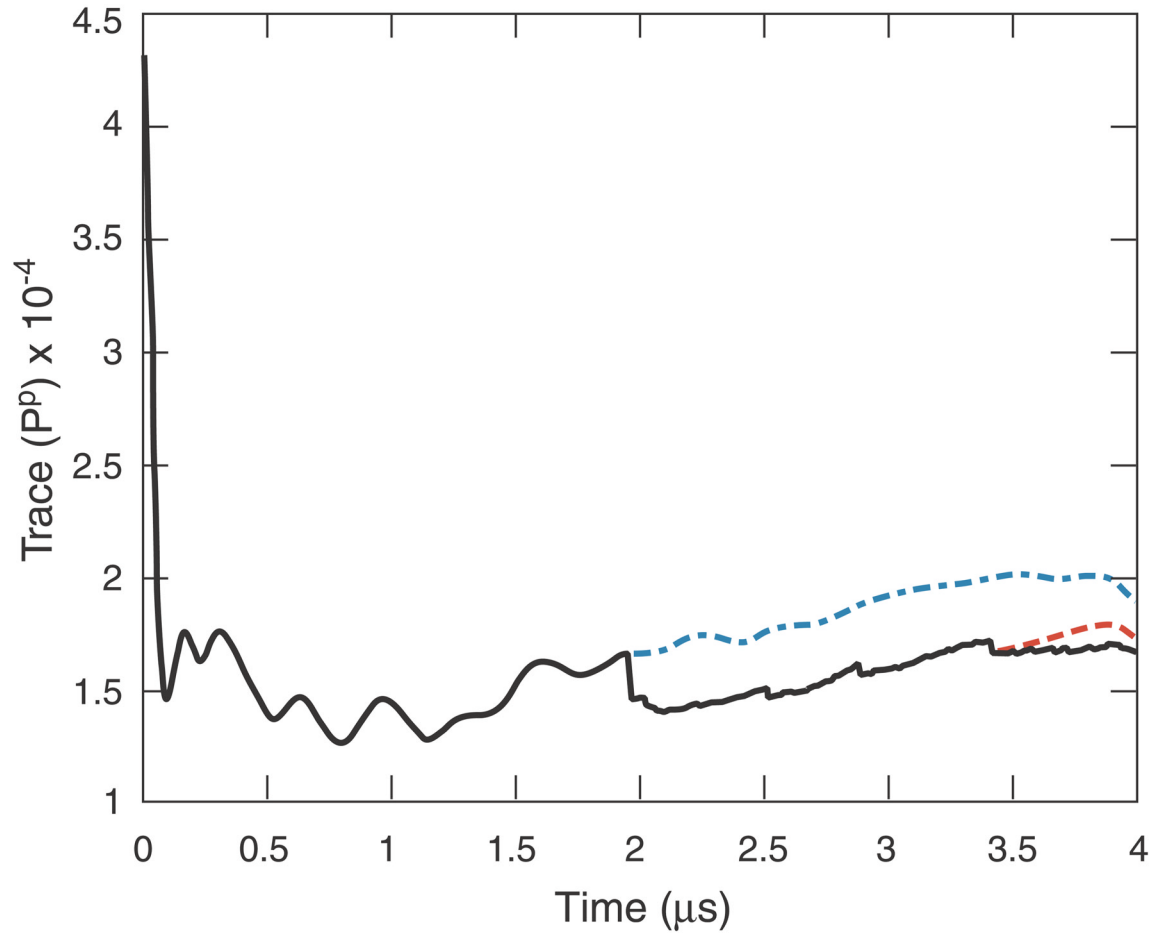


Fig. 6

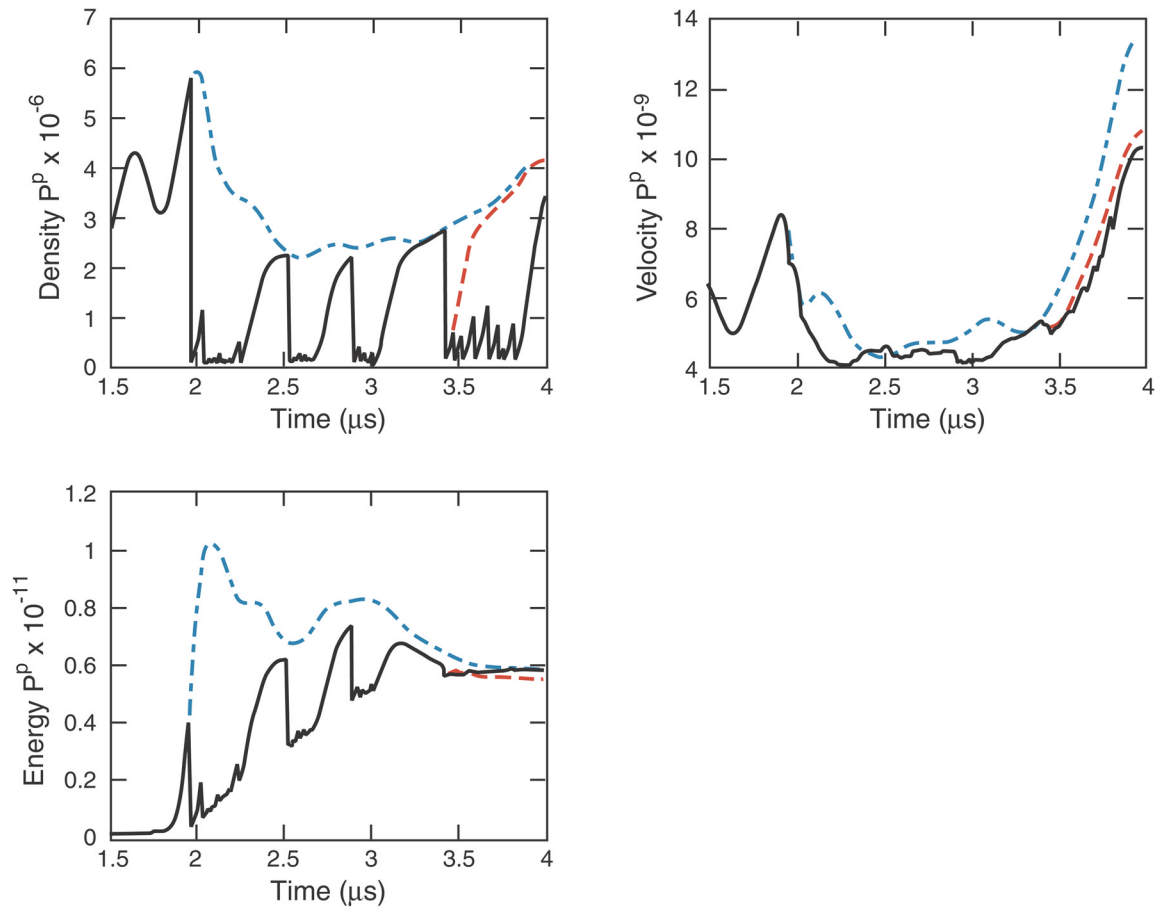


Fig. 7

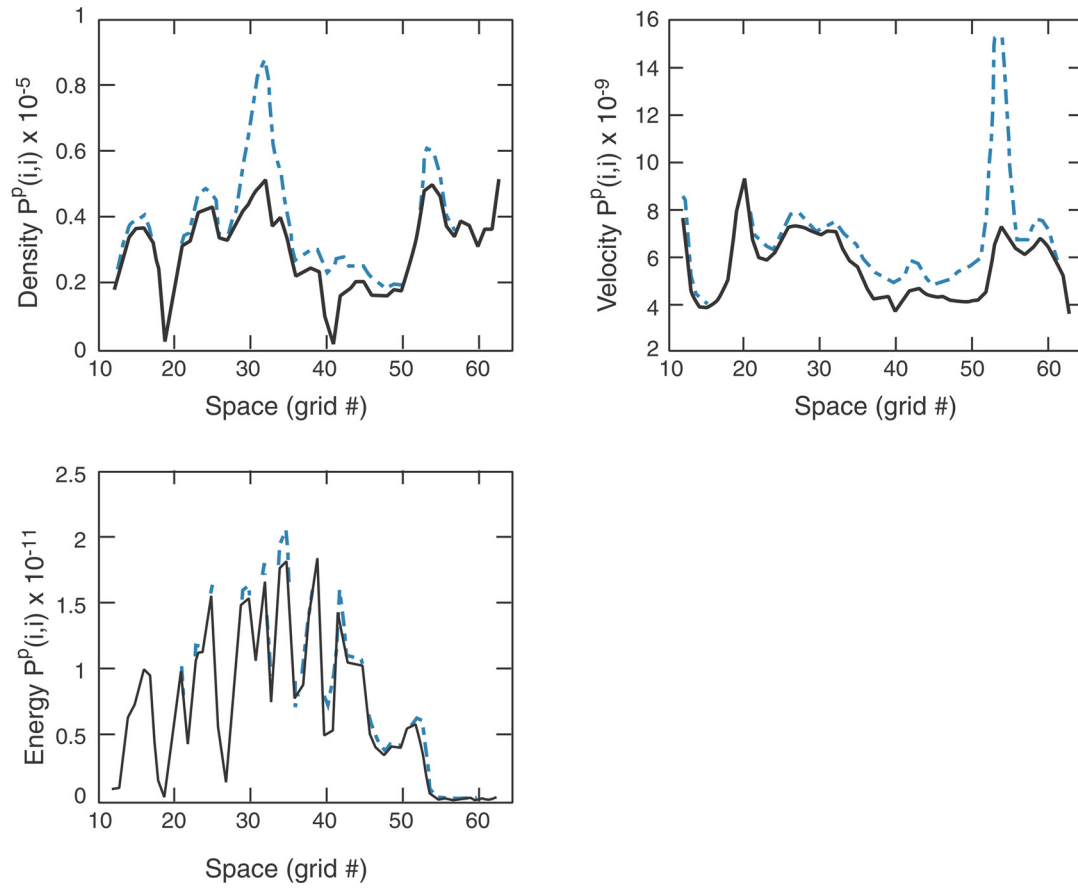


Fig. 8

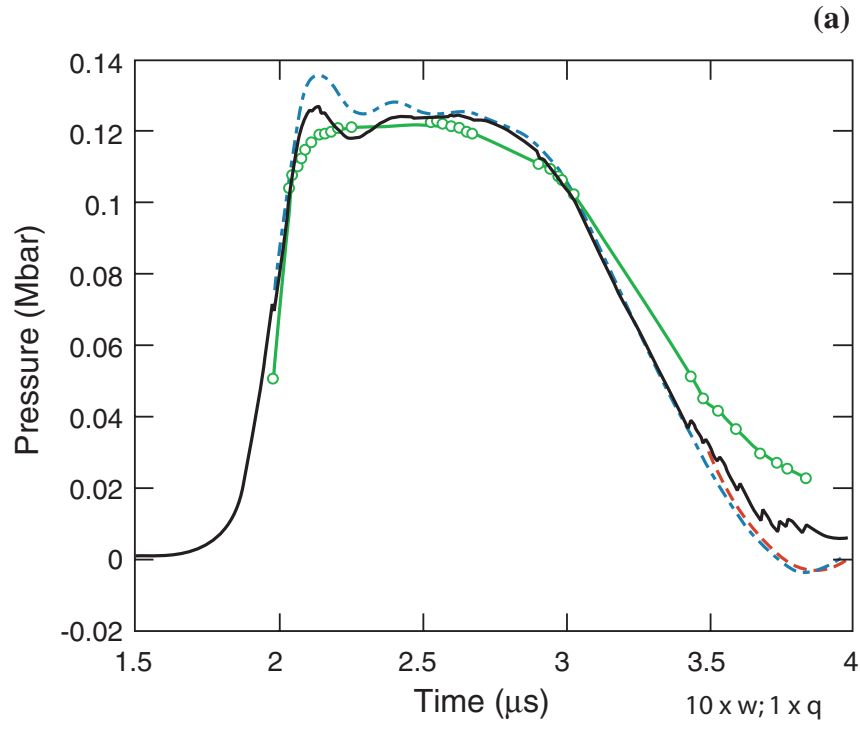


Fig. 9a

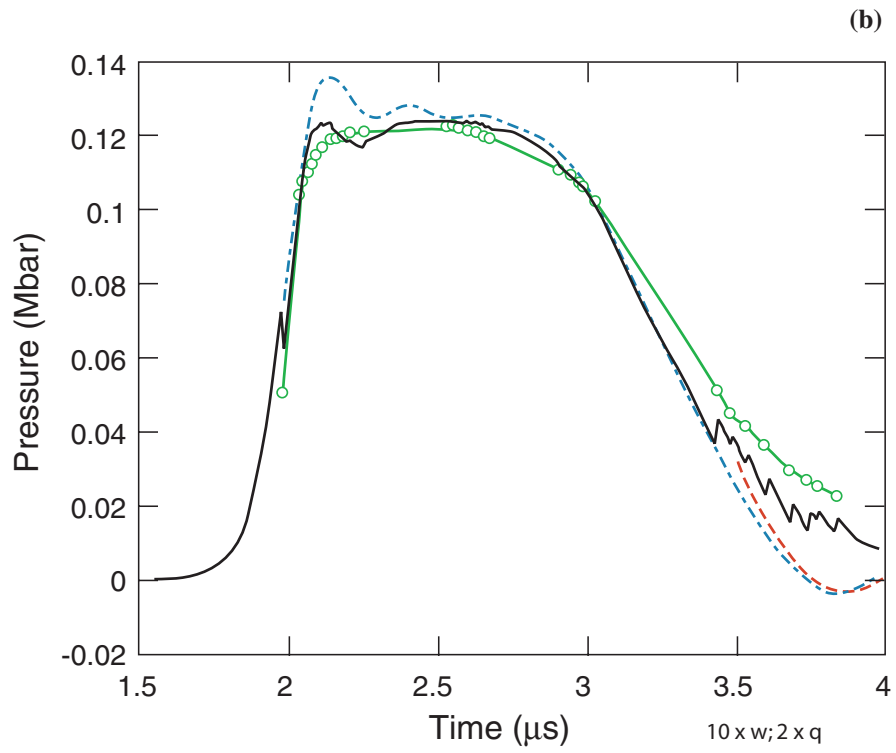


Fig. 9b

continuation of Figure 9

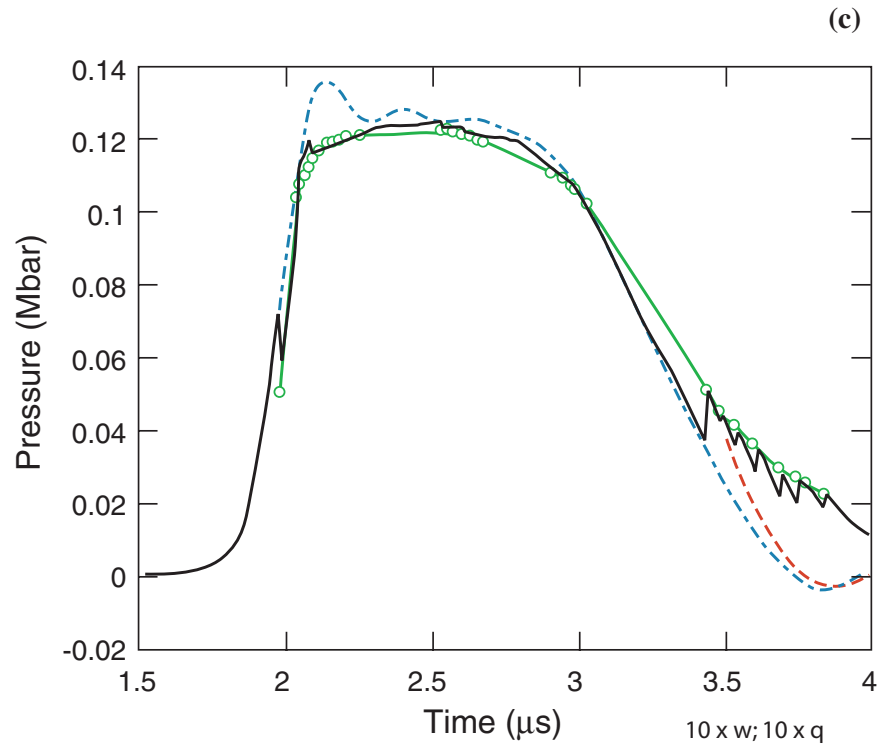


Fig. 9c

Fig. 9

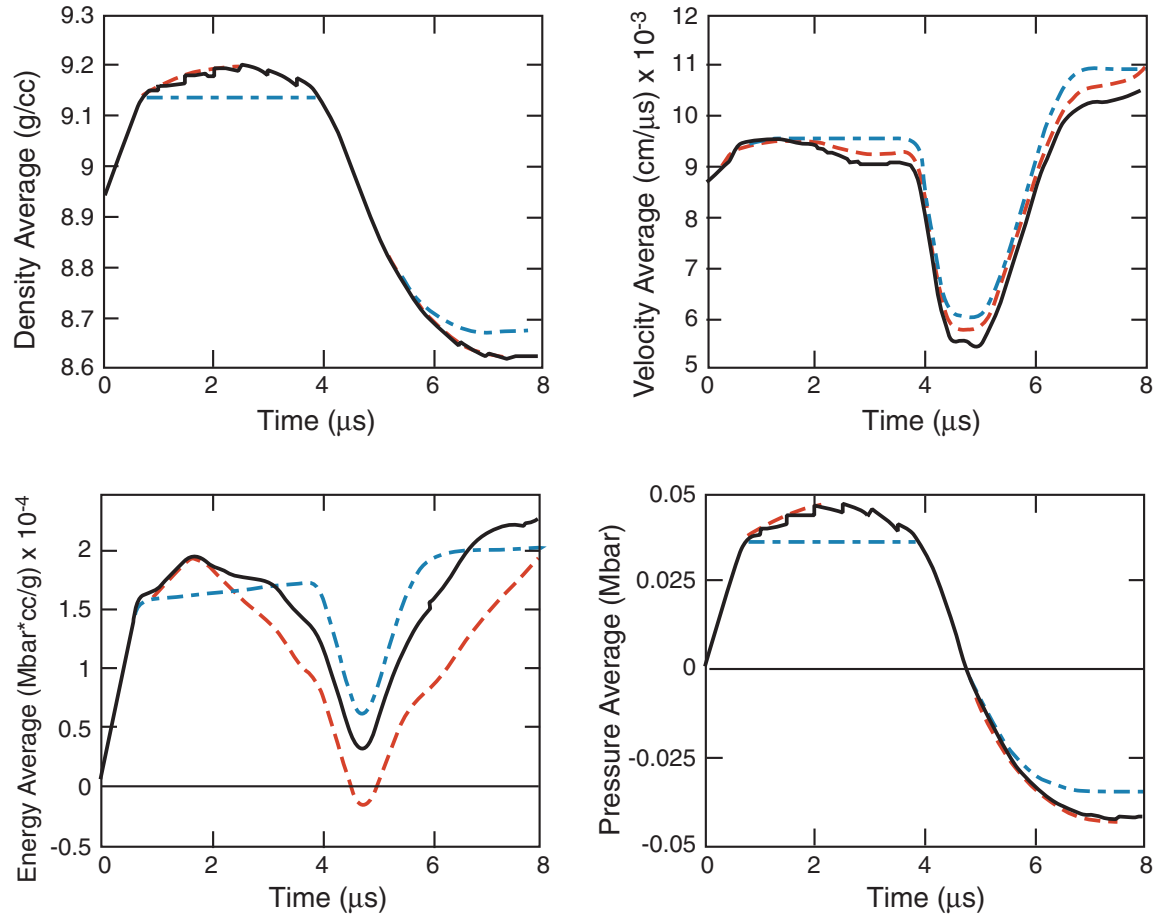


Fig. 10

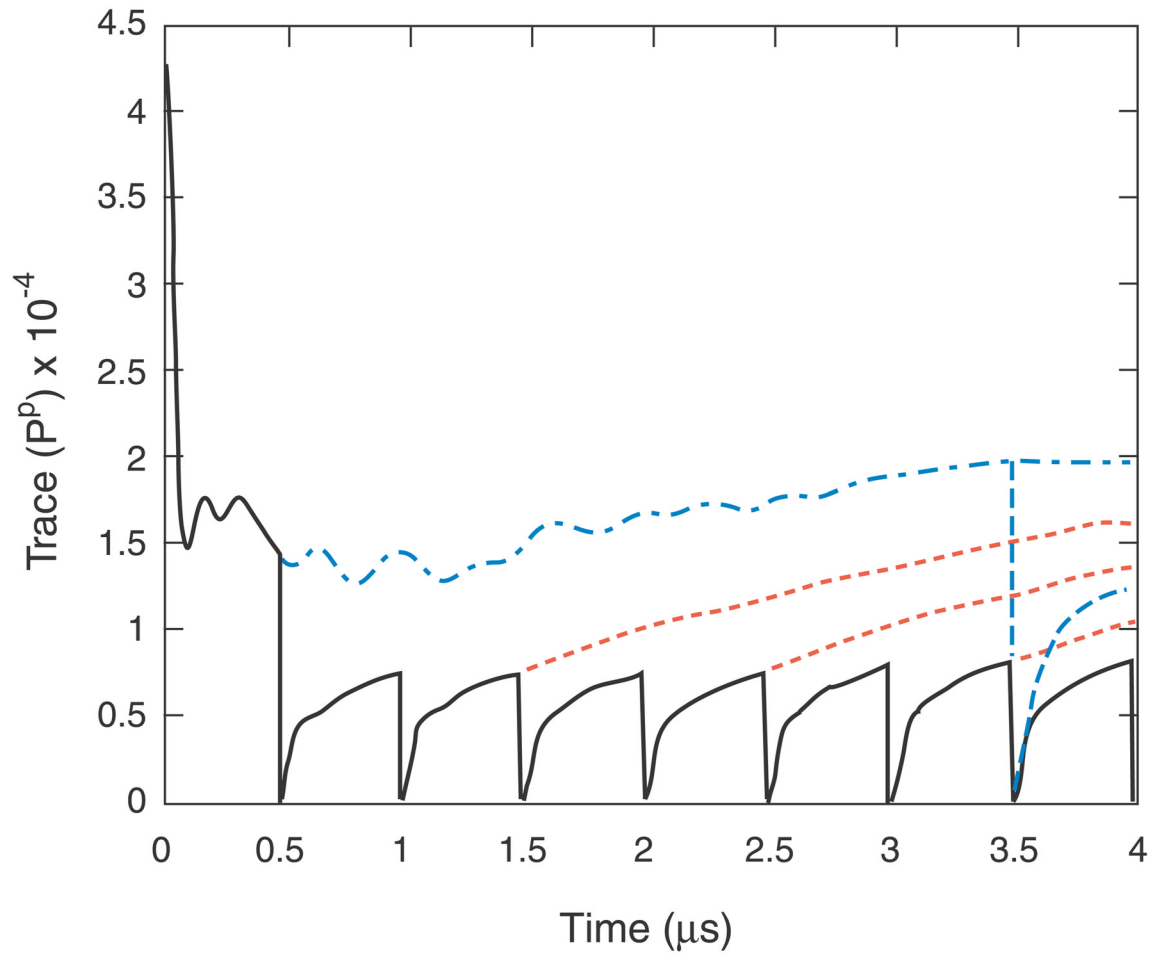


Fig. 11